Measurements and Automated Mechanism Generation Modeling of OH Production in Photolytically Initiated Oxidation of the Neopentyl Radical[||]

Sarah V. Petway,[†] Huzeifa Ismail,[†] William H. Green,*[,†] Edgar G. Estupiñán,[‡,§] Leonard E. Jusinski,[‡] and Craig A. Taatjes[‡]

Department of Chemical Engineering, Massachusetts Institute of Technology, Cambridge, Massachusetts 02139, and Combustion Research Facility, Mail Stop 9055, Sandia National Laboratories, Livermore, California 94551-0969

Received: October 18, 2006; In Final Form: March 21, 2007

Production of OH in the reaction of the neopentyl radical with O_2 has been measured by a laser photolysis/cw absorption method for various pressures and oxygen concentrations at 673, 700, and 725 K. The MIT Reaction Mechanism Generator (RMG) was used to automatically generate a model for this system, and the predicted OH concentration profiles are compared to present and literature experimental results. Several reactions significantly affect the OH profile. The experimental data provide useful constraints on the rate coefficient for the formally direct chemical activation reaction of neopentyl radical with O_2 to form OH $(CH_3)_3CCH_2 + O_2 \rightarrow$ OH + 3,3-dimethyloxetane (Rxn 1) At 673 K and 60 Torr, log k_1 (cm^3 $molecule^{-1}$ s^{-1}) $= -13.7 \pm 0.5$. Absolute absorbance measurements on OH and I indicate that the branching ratio for R + O_2 to OH is about 0.03 under these conditions. The data suggest that the ab initio neopentyl + O_2 potential energy surface of Sun and Bozzelli is accurate to within 2 kcal mol^{-1}.

Introduction

Reactions of alkyl radicals (R) with O_2 are important for understanding low and intermediate temperature hydrocarbon oxidation and autoignition and are especially important in predicting negative temperature coefficient behavior. R + O_2 reactions involve the formation of an alkyl peroxy radical, RO_2, Figure 1. At temperatures above 600 K or so, most RO_2 radicals form HO_2 and the conjugate alkene as the major reaction product. The RO_2 radical can also undergo intramolecular hydrogen abstraction to form a hydroperoxy alkyl radical (QOOH). The principal decomposition pathway of QOOH produces OH and a cyclic ether. The QOOH radical can also undergo a second O_2 addition; the species formed in this reaction leads to the chain branching that drives moderate temperature oxidation chemistry. Because of the many pathways, and the convolution of chemically activated and thermal reactions, it is very difficult to isolate and measure the rates of individual steps. Because the competing formation of a conjugate alkene + HO_2 is impossible in the reaction of the neopentyl radical with O_2, this reaction is used to highlight the pathway shown in bold in Figure 1.

Several experimental and modeling studies have investigated the oxidation of the neopentyl radical. Walker and co-workers[1−3] performed slow-flow reactor experiments to analyze the products of neopentane oxidation and suggested a mechanism to explain their results. Hughes et al.[4−5] measured OH production following pulsed photolysis of neopentyl iodide in the presence of O_2 and derived a rate constant for the isomerization of the neopentyl peroxy radical, assuming that the isomerization was effectively irreversible under their experimental conditions. Curran et al.[6] developed a detailed mechanism for the oxidation of neopentane and compared it to experimental results. They later modified the mechanism on the basis of data from high-pressure flow reactor experiments.[7] DeSain et al.[8] measured production of OH and HO_2 in pulsed-photolytic Cl-initiated neopentane oxidation and rationalized their results using a simple model on the basis of analogous time-dependent master equation calculations for the reaction of *n*-propyl with O_2. Sun and Bozzelli[9] calculated thermochemical and kinetic properties for important species in the oxidation of the neopentyl radical using ab initio and density functional calculations. They reported $\Delta_f H°_{298}$ values for relevant species and calculated high-pressure limit rate constants using canonical transition-state theory and pressure-dependent rate constants using QRRK and master equation analyses.

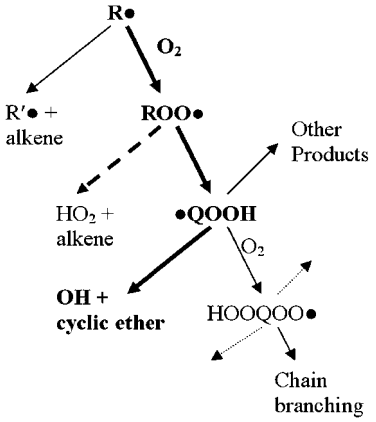

Figure 1. Main reaction pathways for alkyl radicals R• in autoignition. For R = neopentyl, unlike most alkyl radicals, there is no direct route to HO_2. The present work focuses on the reaction path shown in bold.

From comparison of an ad hoc model of neopentyl + O_2 with their measurements of HO_2 and OH formation in Cl-

[||] Part of the special issue "James A. Miller Festschrift".

* To whom correspondence should be addressed. E-mail: whgreen@MIT.edu.

[†] Massachusetts Institute of Technology.

[‡] Sandia National Laboratories.

[§] Present address: Osram Sylvania, Inc., 71 Cherry Hill Drive, Beverly, MA 01915

10.1021/jp0668549 CCC: $37.00
Published on Web 04/18/2007

initiated neopentane oxidation, DeSain et al.[8] concluded that formally direct pathways for chemical activation reactions, especially direct production of OH from R + O_2, are necessary to correctly model neopentane oxidation. The computation of Sun and Bozzelli[9] also included some estimates of these formally direct rate coefficients. Furthermore, reasoning by analogy with *n*-propyl + O_2, for which more detailed calculations were available, DeSain et al.[8] suggested that the "reverse" isomerization of QOOH back to RO_2 was rapid enough to remain significant, if not dominant, in available experimental measurements of neopentyl + O_2, including those of Hughes et al.[4−5] As a result, they questioned the absolute isomerization rate coefficients derived from those prior OH LIF measurements.

In the present work, time-dependent production of OH is measured following pulsed photolysis of neopentyl iodide at various concentrations of O_2 and at temperatures between 673 and 725 K. A mechanism for this system is generated automatically using the MIT Reaction Mechanism Generator (RMG),[10] and predictions of this model are compared to experimental results. Constraints on the rate coefficient for the direct production of OH from R + O_2 are determined from comparison of the model to the experimental data. The experimental data also give information on the main OH-consuming step, reaction (2)

$$OH + C_5H_{11}I \rightarrow \text{products} \qquad \text{(Rxn 2)}$$

The proposed mechanism is also used to model experimental OH profiles in Cl-initiated neopentane oxidation measured by DeSain et al.[8]

Experimental Section

Laser photolysis/transient absorption measurements of product formation in the reaction of neopentyl with O_2 were performed at Sandia National Laboratories, using a method similar to that used in earlier experiments. Neopentyl radical (R) is generated via 266 nm laser photolysis of neopentyl iodide (RI)

$$RI + h\upsilon\ (266\ \text{nm}) \rightarrow I(^2P_{1/2}, ^2P_{3/2}) + R \qquad \text{(Rxn 3)}$$

The production of OH in the neopentyl + O_2 reaction is monitored by direct absorption of OH in the center of the Q_1(2) line of the ($A^2\Sigma$, $\upsilon'=0 \leftarrow X^2\Pi$, $\upsilon''=0$) transition at 307.9951 nm.[11] The detection wavelength is generated using a continuous wave (CW) ring-dye laser pumped by a 532 nm diode-pumped solid-state CW laser. The output of the dye laser is frequency-doubled in a BBO crystal contained in an external cavity, the length of which is actively stabilized to the fundamental laser frequency. The resulting UV laser is split into two beams. The signal from a reference beam (I_0), which does not pass through the cell, is subtracted from that of the beam going through the flow reactor (I) in a low-noise differential amplifier. A variable attenuator on the reference beam is used to maintain equal DC power levels on both detectors. The initial neopentyl radical concentration is determined by measuring the I atom photolysis coproduct. An external-cavity diode laser is used to probe the ($F = 3\ ^2P_{1/2} \leftarrow F = 2\ ^2P_{3/2}$) transition at ~1315 nm.[12] A balanced detection scheme is also incorporated to monitor the transient I atom absorption.

The experiment is carried out in a 1.5 meter long temperature-controlled quartz flow reactor. Calibrated mass flow controllers are used to maintain a constant flow of the reactant and buffer gases. The internal pressure of the reactor is measured by a capacitance manometer and controlled with an automated butterfly valve. A bubbler is used to flow the organic into the reactor using helium as the carrier gas. The flow reactor is heated via three resistive elements that are individually controlled under feedback from three K-type thermocouples to maintain a constant temperature. The experiments were performed at three temperatures (673, 700, and 725 K), two pressures (30 and 60 Torr), and two neopentyl iodide concentrations ([RI] = 2×10^{15} cm^{-3} and 6×10^{15} cm^{-3}, about 2 orders of magnitude greater than $[R]_0$ under these photolysis conditions) Typical oxygen concentrations were varied from 6×10^{16} to 6×10^{17} cm^{-3}, with the remaining total pressure composed of helium.

The [RI] was determined using couple of different approaches. The first method involved using vapor pressure of RI and calculating its mole fraction through the cell based on flows. Because RI vapor pressure was unavailable in the literature, ACD/labs software was used to calculate RI vapor pressure at room temperature.[13] [RI] was also calculated on the basis of the measured photolysis beam absorption. An absorption cross section of 1×10^{-18} cm^2 was used as an estimate for RI at 266 nm on the basis of reported absorption cross sections for iodoethane and 1-iodopropane.[14] The [RI] obtained from UV absorption was about 50% larger than the concentrations estimated on the basis of the ACD/labs vapor pressure formula. Because the UV absorption is a direct measurement of [RI], we chose to use this method in the modeling. But we estimate that this approach still yields an error of about 40% in [RI] on the basis of uncertainties/fluctuations in the photolysis beam power measurement and the uncertainty in the absolute absorption cross section of neopentyl iodide. The principal consequence of this uncertainty is an increased uncertainty in the derived value for the reaction of OH with neopentyl iodide.

The absolute OH concentration is determined using the path length determined from the overlap between photolysis and probe beams (76 cm) and the effective absorption cross section ($\sigma^{ij}_{\text{eff}}(\tilde{\nu})$) for the probed transition

$$\sigma^{ij}_{\text{eff}}(\tilde{\nu}) = n_i \sigma^{ij}_{\text{tot}} F\upsilon(\tilde{\nu}) \qquad (1)$$

where i and j are the lower and upper electronic levels of OH, n_i is the fraction of all the molecules that populate the quantum state i from which transition originates, σ^{ij}_{tot} is the integrated absorption cross section independent of line shape, and $F\upsilon(\tilde{\nu})$ is the normalized Voigt line shape function describing the wavelength dependence of the absorption cross section for the temperature and pressure of the experiments. The σ^{ij}_{tot} for Q_1(2) is 6.479×10^{-16} cm^{-1} cm^2.[15] $F\upsilon$ ($\tilde{\nu}$) can be determined by fitting the temperature and pressure broadening parameters to Voigt profile as outlined by Dorn et al.[15] Absorption by the alkylperoxy radical in this region is negligible.[16]

A similar procedure is used to calculate absolute I atom concentration from the known absorption cross-section of the I atom.[12,17,18] Comparison of the absolute absorptions of I and OH soon after the photolysis pulse allows a determination of the fraction of the initially formed neopentyl radicals being converted to OH.

Modeling Method

Computer programs for the automatic construction of reaction mechanisms have been developed by several groups.[19−28] In this work, we present a model generated by RMG, an open-source, extensible automatic reaction model generation program that combines a rate-based iterative model generation algorithm[29] with the integrated pressure-dependence algorithm developed by Matheu et al.[30] The algorithm is described in detail in ref 10 and briefly summarized here. At the beginning of the model

generation process, only reactants specified in the input file are included in the model; RMG then generates all possible reactions of these species using rate rules stored in a database. The set of ordinary differential equations describing the system is integrated using the stiff ODE integration suite DASPK 3.0,[31] and formation rates of all reaction products not already included in the model are calculated. Each set of reactions of the form A + B → C, B → C, and B → C + D is considered to initiate a pressure-dependent network. These networks are explored by adding one activated isomer at a time. RMG constructs net pressure-dependent reactions from these networks and estimates their rate constants $k(T,P)$. For each pressure-dependent network, a leakage flux is calculated, which represents the flux to all unexplored parts of the network. At each time step, all leakage fluxes and fluxes to possible product species are compared to the minimum formation rate, R_{min}, expressed as

$$R_{min}(t) = \epsilon \cdot R_{char}(t) \quad (2)$$

where ϵ is a user-specified tolerance and the characteristic rate R_{char} is the L2 norm of the reacted species flux vector, $R_{char}(t) = \sqrt{\sum_i R_i^2(t)}$. $R_i(t)$ is the rate of change in the concentration of each species already included in the mechanism. RMG identifies the maximum flux from the formation rates of species not included in the model and fluxes to pressure-dependent networks. If the maximum flux belongs to a chemical species, RMG adds that species to the mechanism with all reactions producing it and generates all possible reactions of that species with other species in the model. If the maximum flux is to a pressure-dependent network, one more activated isomer is added to the network with all its reaction pathways, and rate constants $k(T,P)$ are calculated for all reactions in the network. If all fluxes are less than R_{min}, RMG proceeds to the next time step. Otherwise, the system of ODEs is changed, and the integration starts again at $t = 0$. The mechanism is complete when all fluxes are less than R_{min} at all time points.

RMG estimates pressure-dependent rate constants using a modified version of CHEMDIS, a Quantum Rice−Ramsperger−Kassel/modified strong collision (QRRK/ MSC) code.[32] CHEMDIS calculates $k(T,P)$ using the high-pressure-limit rate constants for all elementary steps in the pressure-dependent network, estimated energy-transfer properties of the bath gas, and densities of states estimated from the heat capacities.

Thermodynamic parameters and high-pressure-limit rate parameters are stored in a hierarchical database based on functional groups. Thermodynamic parameters for specific molecules are included in a primary thermodynamic library, and thermodynamic properties for all other molecules are estimated using group additivity. RMG computes rate constants from rules in a kinetics database that is divided into 34 reaction families. Rate coefficients for some small molecule oxidation reactions that cannot be described by reaction families are included in a primary reaction library. In this work, rate and thermodynamic parameters from Sun and Bozzelli[9] were added to the RMG database. Thermodynamic parameters were added in a primary thermodynamic library, and high-pressure-limit rate rules for elementary reactions were added to the kinetics database. Initial conditions were set so that the initial concentration of the neopentyl radical is equal to the measured initial concentration of the iodine radical.

Although the QRRK/MSC calculation permits rapid evaluation of rate constants for pressure-dependent networks, it may not be accurate enough to provide reliable changes to stationary point energies. To estimate the error from using a QRRK/MSC approach to calculate pressure-dependent rate constants, we performed RRKM master equation calculations based on conventional transition state theory using VariFlex.[52] Structures and frequencies from ref 9 were used for reactants, wells, and transition states. The geometry optimizations were performed at the B3LYP/6-31G(d,p) level. A rigid rotor harmonic oscillator/tight transition state treatment was used to evaluate the transition state partition functions. Internal rotors were treated classically, using the method suggested by Pitzer & Gwinn to convert the classical total hindered rotor density of states to a rough estimate of the quantum hindered rotor density, and an Eckart tunneling correction was used. An exponential down model is employed for the energy transfer process with a temperature independent value of $<\Delta E_{down}> = 291$ cm^{-1}.

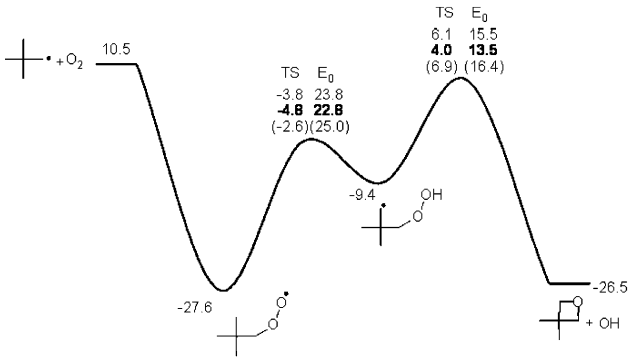

Figure 2. Zero point energy corrected potential energy diagram based on the work of Sun and Bozzelli.[9] Numbers in bold are energies determined in this work from comparison of multiple-well master equation simulations (VariFlex) to experimental data, and numbers in parentheses are those determined from comparison of modified strong-collider (CHEMDIS) calculations to the experiments. Units are kcal mol^{-1}.

Analysis and Discussion

A schematic picture of the potential energy surface for the neopentyl + O_2 reaction based on the work on Sun and Bozzelli[9] is shown in Figure 2. Following the interpretation of DeSain et al.,[8] three pathways can be identified for production of the bimolecular products OH + 3,3-dimethyloxetane in the reaction of neopentyl radical (R) with O_2. One pathway can be termed the "sequential" pathway, namely formation of a stabilized neopentylperoxy (RO_2) molecule (Rxn 4) followed by thermal isomerization to the hydroperoxyalkyl radical QOOH (Rxn 5), which subsequently thermally dissociates into OH + 3,3-dimethyloxetane (Rxn 6).

$$(CH_3)_3CCH_2 + O_2 \rightarrow (CH_3)_3CCH_2OO \quad \text{(Rxn 4)}$$

$$(CH_3)_3CCH_2OO \rightarrow HOOCH_2C(CH_3)_3CH_2 \quad \text{(Rxn 5)}$$

$$HOOCH_2C(CH_3)_3CH_2 \rightarrow OH + \text{3,3-dimethyloxetane} \quad \text{(Rxn 6)}$$

In a kinetic model of this pathway, each intermediate is kinetically significant and hence the production of OH occurs in three kinetically distinct steps. The other two pathways to OH are what DeSain et al.[8] refer to as "formally direct." These pathways are not necessarily "direct" in a dynamical sense, but rather in these pathways one or more of the intermediate species are not kinetically relevant (i.e., its lifetime is much shorter than the time scale on which it is created, and also so short that its bimolecular reactions can be ignored) and hence a correct rate equation model will contain fewer steps from R + O_2 to OH + 3,3-dimethyloxetane. The first of these pathways, and the initial

source of the OH observed in the present experiments, is the formally direct production of OH from R + O_2 (Rxn 1).

$$(CH_3)_3CCH_2 + O_2 \rightarrow OH + \text{3,3-dimethyloxetane} \quad \text{(Rxn 1)}$$

The chemically activated $RO_2^{\#}$ complex formed from the initial R + O_2 encounter has sufficient energy to traverse all transition states between reactants and products,[9] and some fraction of the $RO_2^{\#}$ will produce OH + 3,3-dimethyloxetane without intervening collisional stabilization of the energized neopentylperoxy species. This fraction naturally depends on the pressure. There are similar formally direct, chemically activated reactions R+O_2 → QOOH (Rxn 7) and OH+3,3-dimethyloxetane → RO_2 (Rxn 8). By detailed balance, there are also formally direct pathways for the reverse of each of these 3 reactions. All of these formally direct pathways arise because collisional thermalization of the energized $RO_2^{\#}$ and $QOOH^{\#}$ is relatively slow at the low pressures of the experiments (This effect also causes falloff in the rate constants for reactions 4−6). In the present experiments, OH is formed significantly by reactions 1and 5 and the reverse of reaction 8, and it is consumed primarily by reaction 2.

An additional complication in interpreting these experiments is that the isomerization reactions RO_2 = QOOH are rather fast in this temperature range; in fact, equilibration is computed to be faster than any of the other reaction pathways of either RO_2 or QOOH over the range 400−800 K for the O_2 partial pressures used here. (At low temperatures, R+O_2 can populate the RO_2 well much faster than it can equilibrate with QOOH, whereas at high temperatures, the calculations predict QOOH → OH + cyclic ether can compete effectively with QOOH → RO_2). In the present models, we treat RO_2 and QOOH as kinetically distinct, as the equilibration is predicted to be only modestly faster than the other reactions. But in most kinetics experiments in this temperature range, models indicate that these rapidly equilibrating isomers track each other so closely it might be better to treat them as a single species.

RMG generated a model with 57 species and 881 reactions using a tolerance of $\epsilon = 0.001$. Figure 3 shows predicted and experimental OH concentration profiles at several initial conditions. OH traces for all 36 experimental conditions can be found in the Supporting Information. The predicted OH concentration profiles from the original unadjusted RMG predictions show qualitative agreement with experimental measurements, but the model overestimates the peak OH concentration, and particularly when $[RI]_0$ is large, the peak OH concentration decays faster than is predicted by the model.

Sensitivity analysis was performed to identify the important reactions in this system. RMG automatically calculates first-order sensitivity coefficients using DASPK.[31] Normalized sensitivities of OH are shown in Figure 4. At very early times, the concentration of OH is sensitive only to reaction 1, the formally direct, chemically activated reaction of the neopentyl radical with oxygen producing OH and 3,3-dimethyloxetane. At slightly later times, the OH concentration is most sensitive to reaction 2.

Production of OH from reaction −8 and reaction 6

$$(CH_3)_3CCH_2O_2 \rightarrow OH + \text{3,3-dimethyloxetane} \quad \text{(Rxn −8)}$$

also becomes important at later times after most of the neopentyl radical is consumed. The formation of the stabilized neopentyl peroxy radical (Rxn 4) has a negative sensitivity at early times because this reaction competes with reaction 1; the time constant for the initial rise of OH is essentially the same as the time

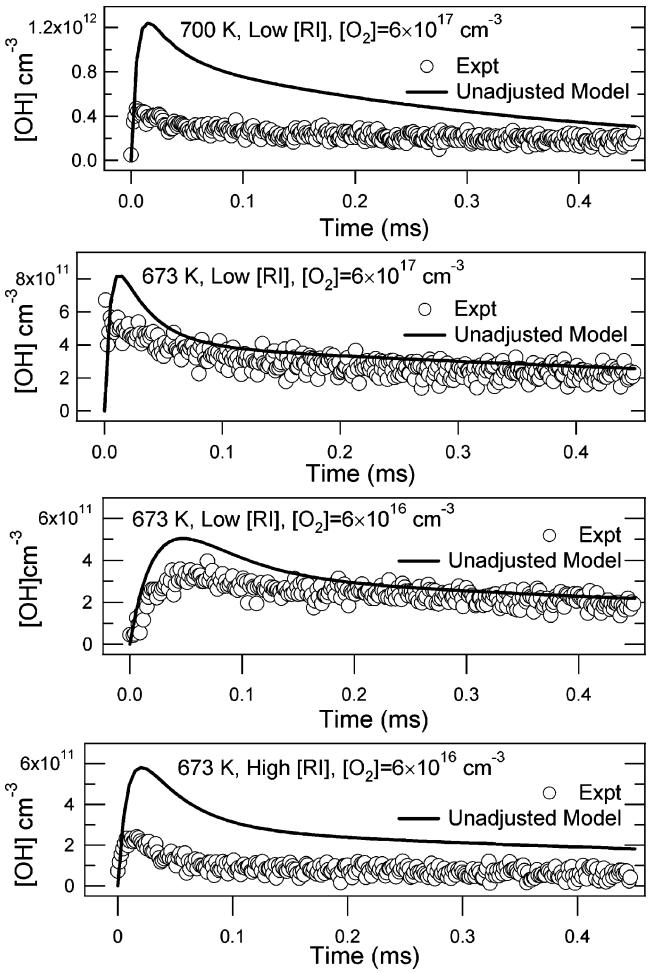

Figure 3. Experimental and predicted OH concentration profiles using unadjusted prior model parameters. Only every 25th experimental point is displayed for clarity.

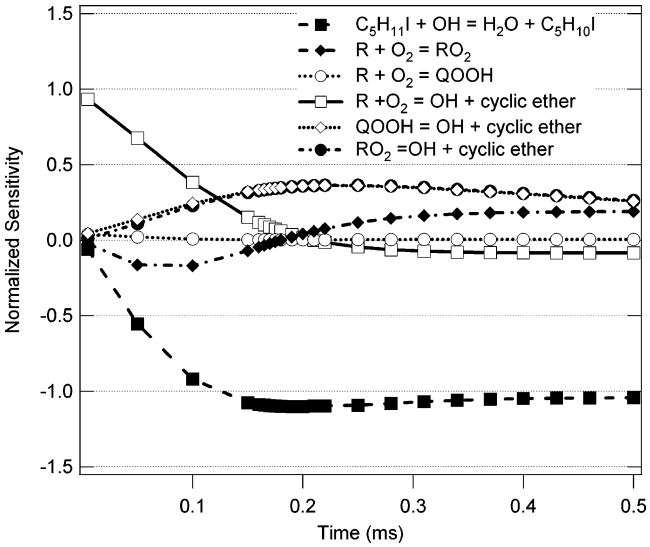

Figure 4. Normalized sensitivities of OH for unadjusted prior kinetic model.

constant for the decay of neopentyl radical via reaction 4. It should be noted that increasing the high-pressure-limit rate constant for reaction 4 should increase the chemically activated rate constant for reaction 1 because the computation of $k_1(T,P)$ depends on the high-pressure-limit values for this rate constant, but the conventional first-order sensitivity analysis employed here does not capture this effect.

The decay of OH is most sensitive to the reaction of OH with neopentyl iodide, reaction 2. RMG's prior prediction for k_2 is $4.81 \times 10^{-17}\ T^{1.8}\ e^{-0.278\ (\mathrm{kcal/mol})/RT}$ cm^3 molecule^{-1} s^{-1} based on a transition state theory calculation by Cohen[33] for the reaction of OH with neopentane. Cohen's pre-exponential factor of 5.25×10^{-17} is multiplied by 11/12 to correct for the number of reaction sites, yielding $k_2 = 4.8 \times 10^{-12}$ cm^3 molecule^{-1} s^{-1} at 673 K. A recent literature review by Atkinson[34] suggests a rate expression of $1.86 \times 10^{-17}\ T^{2.00}\ e^{-0.41\ (\mathrm{kcal/mol})/RT}$ cm^3 molecule^{-1} s^{-1} for OH + neopentane, which would give slightly higher values for k_2 (5.7×10^{-12} cm^3 molecule^{-1} s^{-1} at 673 K). Both rate expressions agree reasonably well with those given in the literature reviews by Baulch et al.[35] ($7.96 \times 10^{-18}\ T^{2.08} e^{-0.14\ (\mathrm{kcal/mol})/RT}$ cm^3 molecule^{-1} s^{-1}, $k_2(673\ \mathrm{K}) = 5.0 \times 10^{-12}$ cm^3 molecule^{-1} s^{-1}) and Walker et al.[36] ($2.34 \times 10^{-14}\ T^{1.00}\ e^{-1.29\ (\mathrm{kcal/mol})/RT}$ cm^3 molecule^{-1} s^{-1}, $k_2(673\ \mathrm{K}) = 5.5 \times 10^{-12}$ cm^3 molecule^{-1} s^{-1}). Tully et al.[37] measured the rate constant for OH + neopentane using flash photolysis and report a rate expression of $1.09 \times 10^{-20}\ T^{3.02}\ e^{-0.70\ (\mathrm{kcal/mol})/RT}$ cm^3 molecule^{-1} s^{-1} ($k_2(673\ \mathrm{K}) = 2.1 \times 10^{-12}$ cm^3 molecule^{-1} s^{-1}), which is lower than the value calculated by Cohen by approximately a factor of 2. To improve the predicted OH fall and steady-state concentration, RMG's estimate for k_2 was increased by a factor of 2 in the adjusted model. However, uncertainty limits for this rate coefficient derived from the present model (see below) are substantial.

To precisely predict the measured peak OH concentration, it is necessary to adjust the rate constant for Rxn 1 slightly from its value as computed by CHEMDIS from the rate and thermodynamic parameters of Sun and Bozzelli.[9] This might be because of small errors in the computed PES, or because of approximations in the computation of the chemically activated rate constant.

As k_1 depends on thermodynamic parameters and high-pressure-limit rate rules for reactions in the pressure-dependent network, its sensitivity to these parameters was examined. Sensitivities to pre-exponential factors were computed by multiplying the pre-exponential factor of the high-pressure limit rate rule by 2 for both forward and reverse reactions and calculating the change in the pressure-dependent rate constant. Sensitivities to activation energies and heats of formation were similarly estimated by increasing the energy by 1 kcal mol^{-1}, and sensitivities to entropy were calculated by increasing S by 1 cal mol^{-1} K^{-1}.

The pressure-dependent rate constant for Rxn 1 is most sensitive to the pre-exponential factor of Rxn 4. Increasing this parameter by a factor of 2 causes an 80% increase in k_1. Doubling the pre-exponential factor for Rxn 5 causes k_1 to increase by approximately 40%, and increasing its activation energy by 1 kcal mol^{-1} decreases k_1 by 20%. Doubling the pre-exponential factor for Rxn 6 increases k_1 by about 30%, and increasing its activation energy by 1 kcal mol^{-1} causes k_1 to decrease by 25%. The activation energy of the decomposition of QOOH has a larger effect than the activation energy for the isomerization reaction because the energy of the transition state for this reaction is much closer to the energy of the entrance channel. The sensitivity of k_1 to the heat of formation of the RO_2 radical and to the entropies of RO_2 and QOOH is low. Its sensitivity to the heat of formation for QOOH is similar to the sensitivity to the activation energy for the QOOH decomposition, which suggests, not unexpectedly, that the formally direct step from R + O_2 to OH + 3,3-dimethyloxetane is sensitive to the energy of the transition state for QOOH decomposition relative to the energy of R + O_2.

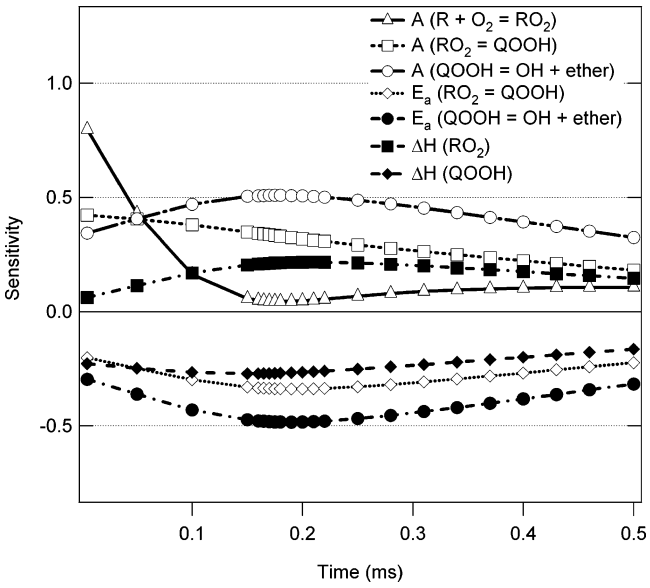

Figure 5. Sensitivity of OH concentration to thermodynamic and high-pressure-limit rate parameters in the pressure-dependent network for unadjusted prior model. Sensitivities to pre-exponential factors are normalized sensitivities ($\Delta \ln [\mathrm{OH}]/\Delta \ln A$). Sensitivities to activation energies and heats of formation are semi-normalized ($\Delta \ln [\mathrm{OH}]/\Delta E_a$ or $\Delta \ln[\mathrm{OH}]/\Delta(\Delta H_f)$) and have units of mol kcal^{-1}.

Because the high-pressure-limit rate constants and thermodynamic parameters in the pressure-dependent network also affect other reactions producing OH, the sensitivity of the OH concentration to these parameters was examined. Sensitivities to heats of formation and high-pressure-limit pre-exponential factors and activation energies are shown in Figure 5. Sensitivities were calculated by changing the pre-exponential factor by a factor of 2 or changing the activation energy or heat of formation by 1 kcal mol^{-1} and observing the change in predicted OH concentration. In the initial time following the photolysis, the OH concentration is most sensitive to the pre-exponential factor for Rxn 4, but the pre-exponential factors and activation energies for Rxns 5 and 6 and the heat of formation for QOOH are also important at early times. The sensitivity to Rxn 4 decreases quickly and becomes lower than the sensitivity to the heat of formation for RO_2 after about 0.1 ms.

Rate and thermodynamic parameters in the pressure-dependent network were varied to determine the combination of parameters that gives the best qualitative agreement with experimental data. Increasing the activation energy of the QOOH decomposition by 0.8 kcal/mol and increasing the activation energy of the RO_2 isomerization by 1.2 kcal/mol gave the best agreement with experimental data because the model is sensitive to these parameters in the region where the unadjusted model disagrees with experiment. Figure 6 shows a comparison of the observed OH profiles with model predictions using the adjusted values of the rate constants. The complete mechanism generated by RMG, with the adjusted rate constants, is supplied as Supporting Information. The model predictions match the experimental time-dependent profiles very well. The current model also gives nearly perfect agreement with the experimental time profile published by Hughes et al.[5] A comparison of the model with their data can be found in the Supporting Information. Predicted concentration profiles for other major species are shown in Figure 7. Most of the neopentyl radical reacts with oxygen to produce RO_2, but smaller fractions go directly to QOOH and to OH + 3,3-dimethyloxetane. Most of the QOOH radical is produced directly from neopentyl + O_2 in a chemically activated process; the QOOH and RO_2 formed initially then

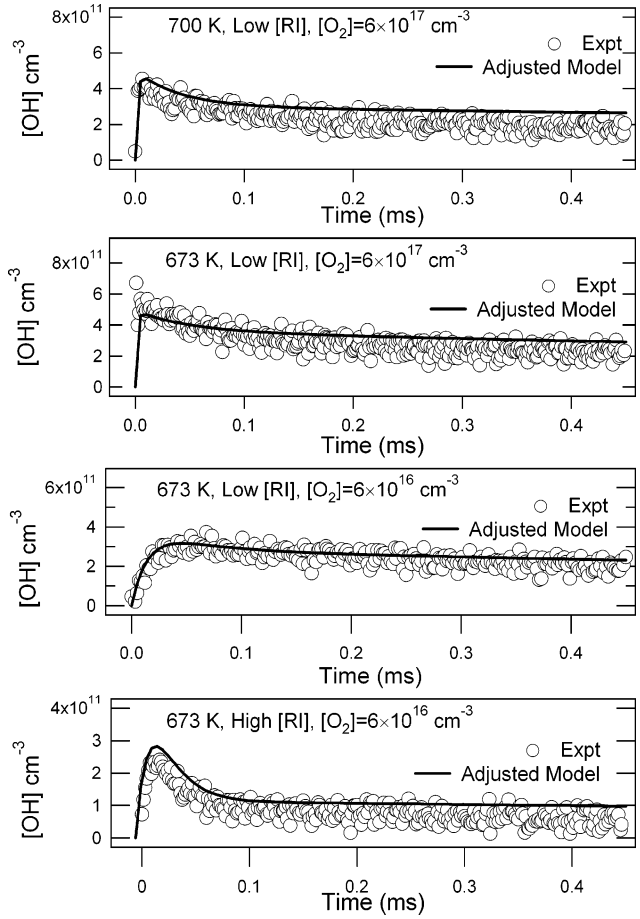

Figure 6. Predicted and experimental OH concentration profiles using the best model (adjusted transition state energies for computing k_1 and adjusted k_2).

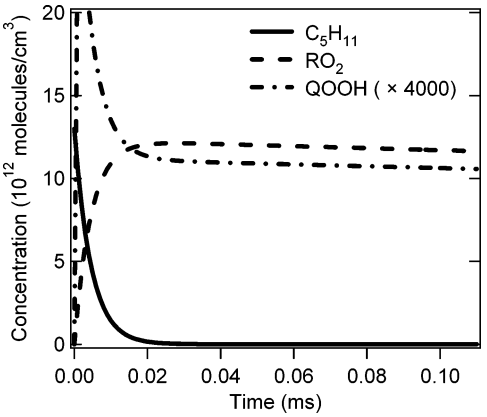

Figure 7. Predicted concentration profiles for C_5H_{11}, $C_5H_{11}O_2$, and QOOH. Initial conditions are 673 K, 60 Torr, $[O_2]_o = 6 \times 10^{17}$ cm^{-3}, $[RI]_o = 9 \times 10^{14}$ cm^{-3}, $[R]_o = [I]_o = 1.4 \times 10^{13}$ cm^{-3}.

come into quasi-equilibrium on a somewhat longer time scale. A small fraction of QOOH is consumed in Rxn 6.

To quantify the constraints placed on individual rate coefficients by modeling the data, it is necessary to propagate the uncertainties in the rate parameters to variation in the model predictions. As an estimate of the maximum uncertainty on the OH predictions, all high-pressure-limit rate constants were changed to their upper or lower bounds on the basis of the sign of the sensitivity coefficient. Uncertainties in the rate constants for the primary reaction library were taken from the literature[38−51] or estimated when literature values were not available. The error bounds for the rate constants that are computed by application

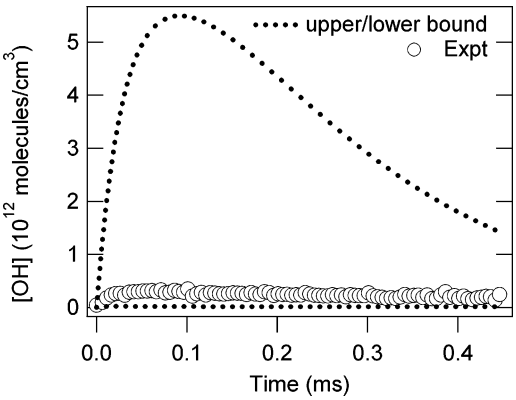

Figure 8. Prior uncertainty in model predictions of OH concentration, based on the large uncertainties in rate constant estimates previous to this work. These experiments provide the information needed to considerably narrow these uncertainty ranges. Initial conditions are 673 K, 60 Torr, $[O_2]_o = 6 \times 10^{16}$ cm^{-3}, $[RI]_o = 9 \times 10^{14}$ cm^{-3}, $[R]_o = [I]_o = 1.4 \times 10^{13}$ cm^{-3}. Only every 100th experimental point is shown for clarity.

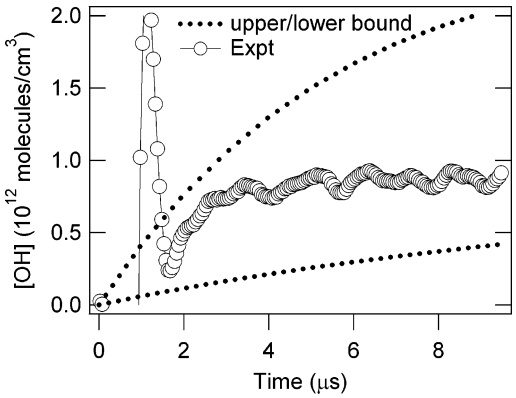

Figure 9. Bounds on predicted OH concentration at early times using experimentally determined k_1. Upper and lower bounds on k_1 were calculated so that all experimental data points are within the error bounds on the predicted OH concentration for every possible variation of rate constants for all other reactions in the model, within the uncertainties in their RMG estimates. The dotted lines are upper and lower bounds on OH predictions using these newly determined (conservative) bounds on k_1, and circles are experimental data. The large excursions at very early time arise from electronic noise and are not included in the fit.

of reaction-family rules are estimated to be a factor of 2 in the pre-exponential factor and 2 kcal mol^{-1} in the activation energy. Uncertainties in the high-pressure-limit rate parameters from Sun and Bozzelli were also estimated as a factor of 2 for pre-exponential factors and 2 kcal/mol^{-1} for activation energies. These relatively large a priori uncertainties result in the upper and lower bounds on the predicted OH profile shown in Figure 8. These bounds are maximum excursions of the OH prediction and are substantial overestimates of the uncertainty as usually defined because they correspond to the unlikely event that all rate coefficients are incorrect by their 95% uncertainties and that all rate coefficient errors are correlated to affect the OH profile most. To determine which reactions contribute most to the model uncertainty, the contribution of each rate constant to the total uncertainty was estimated as the product of the sensitivity coefficient and uncertainty in the rate constant. Before 10 μs, virtually all of the uncertainty is from the rate constant for Rxn 1, the formally direct reaction producing OH and 3,3-dimethyloxetane, implying that the present data can be used to narrow the error bar on this rate coefficient. At later times, over

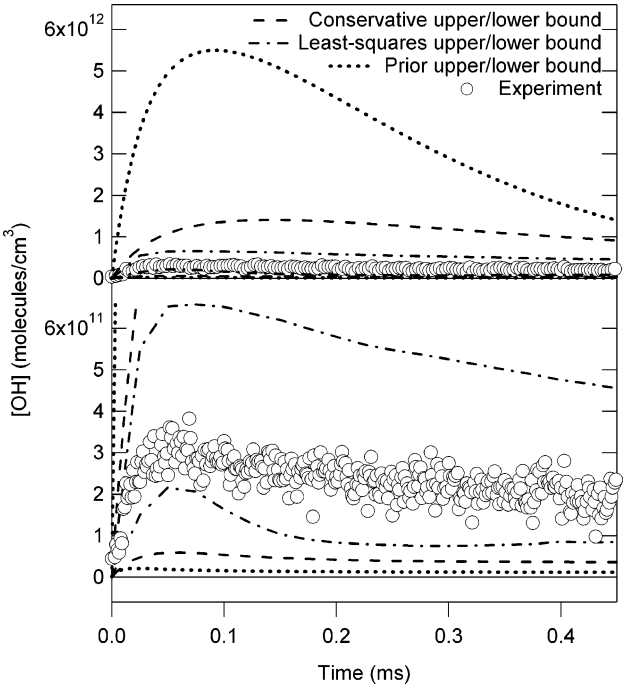

Figure 10. Improved uncertainty estimates for OH predictions using the new experimental data, shown on two vertical scales. The large error bounds calculated using only information available prior to these experiments are shown as the dotted lines. The two tighter error bounds (conservative bounds correspond to the maximum excursion and least-squares bounds correspond to 95% level bounds assuming uncorrelated errors in rate constants) use the new experimentally determined error bounds on k_1 and k_2 (in conjunction with the RMG uncertainties for all other reactions). Initial conditions are 673 K, 60 Torr, $[O_2]_0 = 6 \times 10^{16}$ cm^{-3}, $[RI]_0 = 9 \times 10^{14}$ cm^{-3},$[R]_0 = [I]_0 = 1.4 \times 10^{13}$ cm^{-3}.

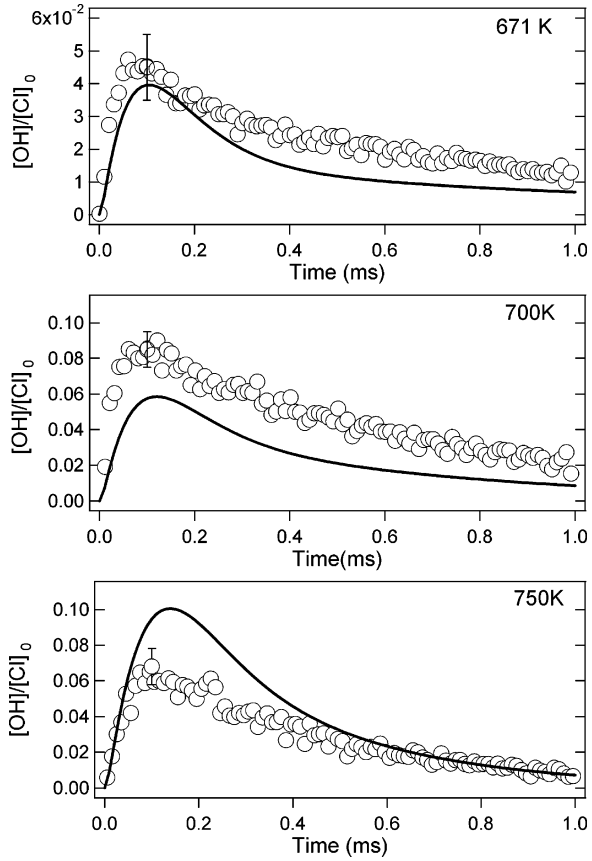

Figure 11. Predicted and experimental OH concentration profiles for Cl-initiated neopentane oxidation using parameter values adjusted to match the RI photolysis experiments. Solid lines are model predictions, and symbols are experimental data. Representative experimental uncertainties in the observed peak OH concentration are shown.

half of the uncertainty is from the rate constant for Rxn 2, the hydrogen abstraction from neopentyl iodide by OH.

Because the OH production at early times is sensitive to reaction 1, upper and lower bounds on that rate constant could be determined using the present experimental data. To quantify the constraints placed on k_1 by the present data, upper and lower bounds on k_1 were first found so that all experimental data points were within the error bounds on the predicted OH concentration at times less than 10 μs. Figure 9 shows upper and lower bounds on the OH predictions using these experimentally determined bounds on k_1. Because this criterion requires all of the data points to lie within the error bounds, and it accounts in the most pessimistic way for all the uncertainties in many other parameters of the large RMG kinetic model, this method gives rather conservative estimates for the limits on k_1. More conventional 95% uncertainties were also determined from the standard deviation calculated from a least-squares fit of the data at early times. Table 1 shows the conservative estimates of the error bounds on k_1 compared with those determined from the conventional least-squares fit. From Table 1, it appears that k_1 may increase slightly with T and P, as predicted by Sun and Bozzelli, but this increase is too small to reliably extract from the experimental data. All the traces at all T and P are consistent with $\log(k_1)$ (cm^3 molecule^{-1} s^{-1}) $= -13.7 \pm 0.5$. The experimental ratio [OH]/[I] at early times indicates that about 3% of the R + O_2 reactions directly form OH, i.e., $k_1/k_4 \approx 0.03$.

Because most of the uncertainty at late times comes from the reaction of neopentyl iodide with OH, error bounds on that rate constant (k_2) can be estimated as well. Upper and lower bounds on k_2 were found so that all data points and errors from other reactions were within the error bounds on the model predictions at times greater than 0.3 ms. Because the modeled OH concentration is also sensitive to other uncertain reactions in this time region, the experimentally derived error bounds are still relatively large. Figure 10 shows the predicted upper and lower limits for the modeled OH concentration using experimentally determined error bounds on the two most sensitive rate constants compared with that calculated from estimated uncertainties in the RMG database. Figure 10 also shows 95% uncertainty limits on the OH prediction assuming uncorrelated errors in the uncertainties of the individual rate coefficients. Using the new experimentally determined values for k_1 and k_2

TABLE 1: Upper and Lower Bounds on k_1 (cm^3 molecule^{-1} s^{-1})

T (K)	P (Torr)	upper bound (conservative)	lower bound (conservative)	upper 95% uncertainty limit (least-squares)	lower 95% uncertainty limit (least-squares)
673	60	4.12×10^{-14}	6.36×10^{-15}	2.49×10^{-14}	1.32×10^{-14}
700	60	4.55×10^{-14}	8.42×10^{-15}	3.11×10^{-14}	1.45×10^{-14}
725	60	5.53×10^{-14}	1.21×10^{-14}	5.48×10^{-14}	1.63×10^{-14}
673	30	3.82×10^{-14}	6.36×10^{-15}	3.12×10^{-14}	1.16×10^{-14}
700	30	5.61×10^{-14}	1.00×10^{-14}	4.53×10^{-14}	1.23×10^{-14}
725	30	6.23×10^{-14}	1.01×10^{-14}	4.2×10^{-14}	1.73×10^{-14}

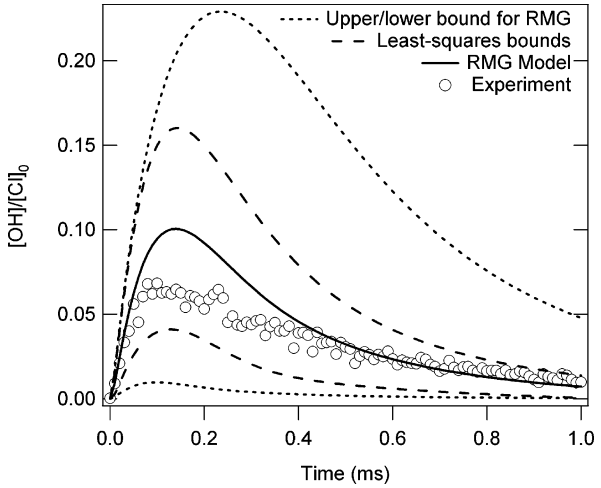

Figure 12. Maximum excursions (upper and lower bounds) and 95% uncertainty limits (least-squares bounds, assuming uncorrelated errors) on OH predictions for Cl-initiated neopentane oxidation at 750 K, using experimentally determined uncertainty in k_1 in conjunction with the uncertainties in the RMG estimates of other reactions.

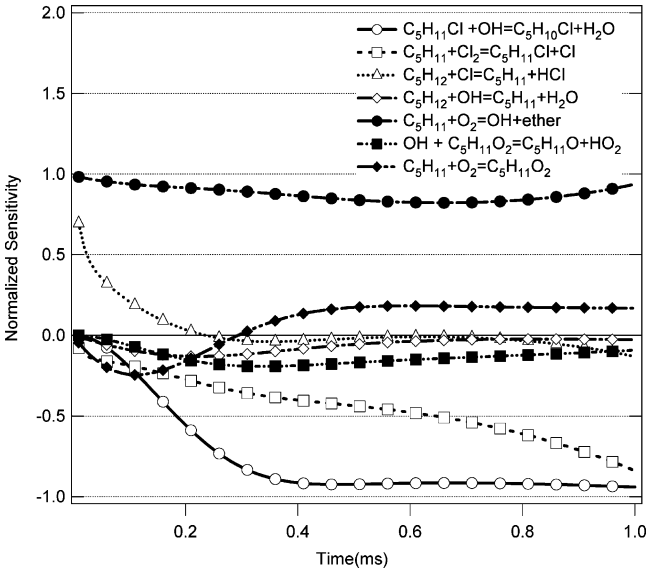

Figure 13. Normalized sensitivities of OH in Cl-initiated neopentane oxidation at 750 K using model with adjusted parameters from neopentyl iodide experiments.

rather than the initial very uncertain RMG estimates for these reactions substantially reduces the uncertainty in the predicted OH concentration profile. Our best-fit estimate is $\log(k_2)$ (cm^3 $molecule^{-1}$ s^{-1}) $= -11.0 \pm 0.4$.

The production of OH in chlorine-initiated neopentane oxidation was also modeled using initial conditions described in the experimental investigation by DeSain et al.[8] Rate constants from DeSain et al. were added to the RMG database for important reactions involving chlorine. The model uses adjusted values of the activation energies determined from modeling the neopentyl iodide experiments. A comparison of predicted and experimental OH profiles is shown in Figure 11 for several temperatures. The model agrees with experimental observations reasonably well. Error bounds on the model prediction at 750 K are shown in Figure 12. Error bounds were calculated using the experimentally determined error bars for k_1 and estimated uncertainties in the RMG database for all other reactions.

Figure 13 shows normalized sensitivities of OH as a function of time for the most sensitive reactions in this system. As in the neopentyl iodide system, the OH concentration in chlorine-initiated neopentane oxidation is very sensitive to the formally direct reaction of oxygen with the neopentyl radical producing OH and 3,3-dimethyloxetane, but the sensitivity to this reaction remains high at later times. The concentration of OH in this system is also sensitive to

$$C(CH_3)_4 + Cl \rightarrow (CH_3)_3CCH_2 + HCl \quad \text{(Rxn 9)}$$

The sensitivity to Rxn 4 is similar to its sensitivity in the neopentyl iodide system. The decay of OH is most sensitive to

$$(CH_3)_3CCH_2Cl + OH \rightarrow (CH_3)_2C(CH_2)CH_2Cl + H_2O \quad \text{(Rxn 10)}$$

but OH is also consumed by

$$C(CH_3)_4 + OH \rightarrow (CH_3)_3CCH_2 + H_2O \quad \text{(Rxn 11)}$$

and

$$(CH_3)_3CCH_2O_2 + OH \rightarrow (CH_3)_3CCH_2O + HO_2 \quad \text{(Rxn 12)}$$

At later times, the concentration of OH becomes sensitive to

$$(CH_3)_3CCH_2 + Cl_2 \rightarrow (CH_3)CCH_2Cl + Cl \quad \text{(Rxn 13)}$$

which competes with the direct reaction with O_2 producing OH. The concentration of OH is more sensitive to Rxn 10 than to Rxn 11 because as neopentane is consumed in reaction 10, the concentration of neopentyl chloride produced in Rxn 13 becomes higher than the concentration of neopentane.

RMG was also used to model the neopentane oxidation experiments of Walker and co-workers.[2] The model was generated at 480 °C, and initial partial pressures of H_2, O_2, and neopentane were 425, 70, and 5 Torr. Measured mole fractions of 3,3-dimethyloxetane, C_4H_8, CO, CH_2O, and CH_4 differ from RMG predictions by less than a factor of 3 and are within the error bounds on model predictions at 10 and 20% neopentane conversion. Reactions contributing most to the uncertainty in model predictions at these conditions include

$$C(CH_3)_4 + HO_2 \rightarrow (CH_3)_3CCH_2 + H_2O_2 \quad \text{(Rxn 14)}$$

$$(CH_3)_3CCH_2 \rightarrow CH_3 + C_4H_8 \quad \text{(Rxn 15)}$$

$$\text{3,3-dimethyloxetane} \rightarrow C_4H_8 + CH_2O \quad \text{(Rxn 16)}$$

and Rxn 4 and Rxn 6.

Some of the differences between the experimental results and model predictions may be the result of using a QRRK/MSC approach to estimate pressure-dependent rate constants. The values for $k_1(T,P)$ obtained from the more rigorous master equation analysis, employing the stationary point characteristics as calculated by Sun and Bozzelli,[9] are compared to those calculated using CHEMDIS and those determined experimentally in Figure 14. These results are also compared to rate coefficient results from Sun and Bozzelli,[9] who used a QRRK approach to estimate the microcanonical rate constants and master equation analysis for pressure falloff. Rate constants calculated using VariFlex are lower than those determined experimentally by a factor of 1.5−2, whereas Sun and Bozzelli's calculations are higher than the experimental values by a factor of 2−3. Values of k_1 calculated using CHEMDIS show good agreement with experimental results at 60 Torr but disagree by approximately a factor of 2 at 30 Torr. CHEMDIS estimates and results from Sun and Bozzelli overestimate the pressure-dependence of k_1. Whereas comparison of the experimental data

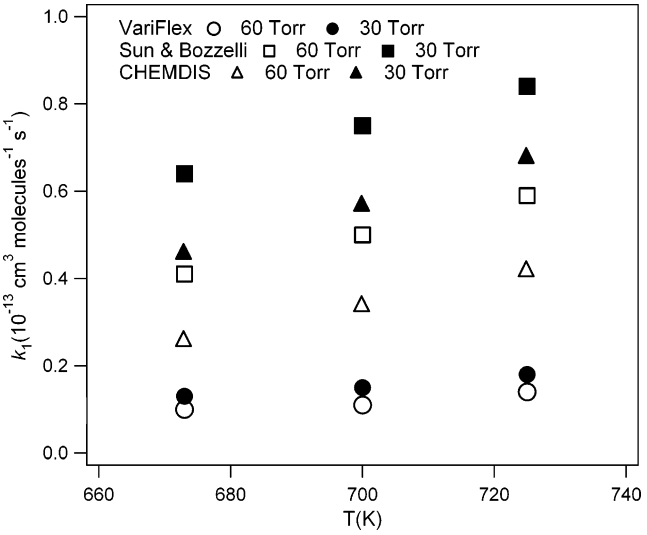

Figure 14. Comparison of $k_1(T,P)$ calculated using a QRRK/MSC approach (CHEMDIS) with master equation results (VariFlex and Sun & Bozzelli[9]). The range in the theoretical predictions (all based on the Sun & Bozzelli ab initio PES) is comparable to the uncertainty range of the experimentally determined k_1.

with the CHEMDIS results suggests higher barriers for the RO_2 isomerization and QOOH decomposition, comparison with the VariFlex calculations suggests these barriers are actually lower than those calculated by Sun and Bozzelli. The energies of these transition states were varied within their estimated uncertainty ranges, and VariFlex simulations were run to determine the barrier heights that gave the best agreement with experimental results. Decreasing the barriers for the RO_2 isomerization and QOOH decomposition by 1 and 2 kcal/mol, respectively, gave the best agreement with the experimentally determined values for k_1. The suggested activation energies and transition-state energies are shown on the potential energy diagram adapted from Sun and Bozzelli (Figure 2). The time-dependent master equation calculation using VariFlex is most accurate but may still be expected to slightly underestimate $k(E)$ because of the classical treatment of the internal rotors. Therefore, it is concluded that E_o for $RO_2 \rightarrow$ QOOH is greater than or equal to 22.8 kcal mol^{-1} and that the transition state for QOOH $\rightarrow$ OH + 3,3-dimethyloxetane is lower than the energy of the entrance channel R + O_2 by no more than 6.5 kcal mol^{-1}.

Conclusions

The transient absorption of OH formed by flash photolysis of neopentyl iodide in the presence of O_2 was measured at temperatures between 673 and 725 K and pressures of 30 and 60 Torr. RMG was used to generate a mechanism for the oxidation of the neopentyl radical. The comparison of this model with the experimental results confirms the importance of the formally direct chemically activated reaction R + $O_2 \rightarrow$ OH + ether for the production of OH. Predicted OH concentration profiles agree with experimental observations reasonably well for the experimental conditions presented in this work and for the conditions described in DeSain et al. for Cl-initiated neopentane oxidation. The results suggest barriers of between 22.8 kcal mol^{-1} and 25.0 kcal mol^{-1} for the isomerization of the neopentyl peroxy radical and between 13.5 kcal mol^{-1} and 16.4 kcal mol^{-1} for decomposition of the hydroperoxy neopentyl radical. The production of OH is most sensitive to the formally direct reaction of the neopentyl radical with O_2 producing OH and 3,3-dimethyloxetane and the reaction of neopentyl iodide with OH. Upper and lower limits on these rate constants are calculated using the comparison of the RMG model to experimental data.

Acknowledgment. This work is supported by the Division of Chemical Sciences, Geosciences, and Biosciences, the Office of Basic Energy Sciences, the U.S. Department of Energy, in part through Grant DE-FG02-98ER14914. Sandia is a multiprogram laboratory operated by Sandia Corporation, a Lockheed Martin Company, for the National Nuclear Security Administration under Contract DE-AC04-94-AL85000.

Supporting Information Available: Experimental OH traces for all reaction conditions. Reaction mechanism generated by RMG for oxidation of the neopentyl radical. Comparison of model predictions with experimental data from Hughes et al.[5] This material is available free of charge via the Internet at http://pubs.acs.org.

Note Added after ASAP Publication. This article was released ASAP on April 18, 2007. This paper is part of the special issue "James A. Miller Festschrift". This was not indicated in the previous version. The corrected version was posted on April 23, 2007.

References and Notes

(1) Baldwin, R. R.; Hisham, M. W. M.; Walker, R. W. *J. Chem. Soc., Faraday Trans.* **1982**, *78*, 1615.
(2) Baker, R. R.; Baldwin, R. R.; Everett, C. J.; Walker, R. W. *Combust. Flame* **1975**, *25*, 285.
(3) Baker, R. R.; Baldwin, R. R.; Walker, R. W. *Combust. Flame* **1976**, *27*, 147.
(4) Hughes, K. J.; Lightfoot, P. D.; Pilling, M. J. *Chem. Phys. Lett.* **1992**, *191*, 581.
(5) Hughes, K. J.; Halford-Maw, P. A.; Lightfoot, P. D.; Turanyi, T.; Pilling, M. J. *Symp. Int. Combust. Proc.* **1992**, *24*, 645.
(6) Curran, H. J.; Pitz, W. J.; Westbrook, C. K.; Hisham, M. W. M.; Walker, R. W. *Symp. Int. Combust. Proc.* **1996**, *26*, 641.
(7) Wang, S. M.; David, L.; Cernansky, N. P.; Curran, H. J.; Pitz, W. J.; Westbrook, C. K. *Combust. Flame* **1999**, *118*, 415.
(8) DeSain, J. D.; Klippenstein, S. J.; Taatjes, C. A. *Phys. Chem. Chem. Phys.* **2003**, *5*, 1584.
(9) Sun, H.; Bozzelli, J. W. *J. Phys. Chem. A* **2004**, *108*, 1694.
(10) Song, J. Building Robust Chemical Reaction Mechanisms: Next Generation of Automatic Model Construction Software. Ph.D. Dissertation, Massachusetts Institute of Technology, Cambridge, MA, 2004. http://hdl.handle.net/1721.1/30058.
(11) Dieke, G. H.; Crosswhite, H. M. *J. Quant. Spectrosc. Radiat. Transfer* **1962**, *2*, 97.
(12) Estupiñán, E. G.; Klippenstein, S. J.; Taatjes, C. A. *J. Phys. Chem. B* **2005**, *109*, 8374.
(13) *ACD/ChemSketch*, version 10.00; Advanced Chemistry Development, Inc.: Toronto, ON, 2006; www.acdlabs.com.
(14) Sander, S.P.; Friedl, R. R.; Golden, D. M.; Kurylo, M. J.; Huie, R. E.; Orkin, V. L.; Moortgat, G. K.; Ravishankara, A. R.; Kolb, C. E.; Molina, M. J.; Finlayson-Pitts, B. J. *Chemical Kinetics and Photochemical Data for Use in Atmospheric Studies. Evaluation Number 14*; Report No. JPL Publication 02-25; Jet Propulsion Laboratory, National Aeronautics and Space Administration: Pasadena, CA, 2002.
(15) Dagaut, P.; Kurylo, M. J. *Int. J. Chem. Kinet.* **1990**, *22*, 1177.
(16) Dorn, H. P.; Neuroth, R.; Hofzumahaus, A. *J. Geophys. Res.* **1995**, *100*, 7397.
(17) Ha, T. K.; He, Y.; Pochert, J.; Quack, M.; Ranz, R.; Seyfang, G.; Thanopoulos, I. *Ber. Bunsen−Ges. Phys. Chem.* **1995**, *99*, 384.
(18) Davis, S.; Mulhall, P.; Bachman, M.; Kessler, W.; Keating, P. *J. Phys. Chem. A* **2002**, *106*, 8323.
(19) Broadbelt, L. J.; Stark, S. M.; Klein, M. T. *Ind. Eng. Chem. Res.* **1994**, *33*, 790.
(20) Broadbelt, L. J.; Stark, S. M.; Klein, M. T. *Comput. Chem. Eng.* **1996**, *20*, 113.
(21) Blurock, E. S. *J. Chem. Inf. Comput. Sci.* **1995**, *35*, 607.
(22) Chevalier, C.; Pitz, W. J.; Melenk, H. *Ber. Bunsen−Ges. Phys. Chem.* **1990**, *94*, 1362.
(23) Chevalier, C.; Pitz, W. J.; Warnatz, J.; Westbrook, C. K.; Melenk, H. *Proc. Combust. Inst.* **1992**, *24*, 93.

(24) Chinnick, S. J.; Baulch, D. L.; Ayscough, P. B. *Chemom. Intell. Lab. Syst.* **1988**, *5*, 39.

(25) Prickett, S. E.; Mavrovouniotis, M. L. *Comput. Chem. Eng.* **1997**, *21*, 1219.

(26) Ranzi, E.; Faravelii, T.; Gaffuri, P.; Sogaro, A. *Combust. Flame* **1995**, *102*, 179.

(27) Valdes-Perez, R. E. *J. Comput. Chem.* **1992**, *13*, 1079.

(28) Warth, V.; Battin-Leclerc, F.; Fournet, R.; Glaude, P. A.; Come, G. M.; Scacchi, G. *Comput. Chem.* **2000**, *24*, 541.

(29) Susnow, R. G.; Dean, A. M.; Green, W. H.; Peczak, P.; Broadbelt, L. F. *J. Phys. Chem. A* **1997**, *101*, 3731.

(30) Matheu, D. M. Integrated Pressure-Dependence in Automated Mechanism Generation: A New Tool for Building Gas-Phase Kinetic Models. Ph.D. Thesis, Massachusetts Institute of Technology, Cambridge, MA, 2002.

(31) Li, S.; Petzold, L. R. *Design of New DASPK for Sensitivity Analysis*; UCSB Technical Report; University of California, Santa Barbara: Santa Barbara, CA, 1999.

(32) Chang, A. Y.; Bozzelli, J. W.; Dean, A. M. *Z. Phys. Chem.* **2000**, *214*, 1533.

(33) Cohen, N. *Int. J. Chem. Kinet.* **1991**, *23*, 397.

(34) Atkinson, R. *Atmos. Chem. Phys.* **2003**, *3*, 2233.

(35) Baulch, D. L.; Bowers, D. G.; Malcolm, D. G.; Tuckersman, R. T. *J. Phys. Chem. Ref. Data* **1986**, *15*, 465.

(36) Walker, R. W. *Int. J. Chem. Kinet.* **1985**, *17*, 573.

(37) Tully, F. P.; Koszykowski, M. L.; Binkley, J. S. *Symp. Int. Combust. Proc.* **1985**, *20*, 715.

(38) Atkinson, R.; Baulch, D. L.; Cox, R. A.; Hampson, R. F., Jr.; Kerr, J. A.; Rossi, M. J.; Troe, J. *J. Phys. Chem. Ref. Data* **1997**, *26*, 521.

(39) Atkinson, R.; Baulch, D. L.; Cox, R. A.; Hampson, R. F., Jr.; Kerr, J. A.; Rossi, M. J.; Troe, J. *J. Phys. Chem. Ref. Data* **1997**, *26*, 1329.

(40) Baulch, D. L.; Cobos, C. J.; Cox, R. A.; Frank, P.; Hayman, G.; Just, T.; Kerr, J. A.; Murrells, T.; Pilling, M. J.; Troe, J.; Walker, R. W.; Warnatz, J. *J. Phys. Chem. Ref. Data* **1994**, *23*, 847.

(41) Baulch, D. L.; Cobos, C. J.; Cox, R. A.; Esser, C.; Frank, P.; Just, T.; Kerr, J. A.; Pilling, M. J.; Troe, J.; Walker, R. W.; Warnatz, J. *J. Phys. Chem. Ref. Data* **1992**, *21*, 411.

(42) Tsang, W. *J. Phys. Chem. Ref. Data* **1991**, *20*, 221.

(43) Tsang, W. *J. Phys. Chem. Ref. Data* **1990**, *19*, 1.

(44) Tsang, W. *J. Phys. Chem. Ref. Data* **1998**, *17*, 887.

(45) Tsang, W. *J. Phys. Chem. Ref. Data* **1997**, *16*, 471.

(46) Tsang, W.; Hampson, R. F. *J. Phys. Chem. Ref. Data* **1986**, *15*, 1087.

(47) Sumathi, R.; Carstensen, H. H.; Green, W. H. *J. Phys. Chem. A* **2001**, *105*, 6910.

(48) Sumathi, R.; Carstensen, H. H.; Green, W. H. *J. Phys. Chem. A* **2001**, *105*, 8969.

(49) Sumathi, R.; Carstensen, H. H.; Green, W. H. *J. Phys. Chem. A* **2002**, *106*, 5474.

(50) Sumathi, R.; Green, W. H. *Theor. Chem. Acc.* **2002**, *108*, 187.

(51) Wijaya, C. D.; Sumathi, R.; Green, W. H. *J. Phys. Chem. A* **2003**, *107*, 4908.

(52) Klippenstein, S. J.; Wagner, A. F.; Dunbar, R. C.; Wardlaw, D. M.; Robertson, S. H.; Miller, J. A. *VariFlex*, 1.13m ed.; Argonne National Laboratory: Argonne, IL, 2002.